Lens-free coherent modulation imaging with collimated illumination

Hua Tao (陶 华)[1,3], Suhas P. Veetil[2], Xingchen Pan (潘兴臣)[1,3], Cheng Liu (刘 诚)[1], and Jianqiang Zhu (朱健强)[1,*]

[1]*Shanghai Institute of Optics and Fine Mechanics, Chinese Academy of Sciences, Shanghai 201800, China*
[2]*Department of Engineering Technology and Science, Higher Colleges of Technology, Fujairah 4114, United Arab Emirates*
[3]*University of Chinese academy of sciences, Beijing 100049, China*
**Corresponding author: jqzhu@siom.ac.cn*

Received February 27, 2016; accepted May 16, 2016; posted online June 21, 2016

We propose a lens-free coherent modulation imaging (CMI) method for reconstructing a general complex-valued wave field from a single frame of a diffraction pattern. A numerical Fourier transform is introduced in the iterative reconstruction process to replace the lens or zone plate used in the current CMI technique to adopt the constraint on the Fourier components of the exit wave field of the sample. While the complexity of the experimental setup is remarkably reduced by replacing the zone plate and additional accessories with the numerical processing, the energy fluence loss induced by the undesired diffraction orders of the zone plate can be also avoided. The feasibility of the proposed technique is verified experimentally with visible light.

OCIS codes: 100.5070, 050.1970, 120.5050, 070.0070.
doi: 10.3788/COL201614.071203.

Phase retrieval technology has attracted much attention in recent years, owing to its significant contribution in several applications of many areas, such as the materials science[1–3], biology[4], and physics[5–7], where it is effectively used for the high-contrast imaging or wavefront sensing[8–10]. Coherent diffraction imaging (CDI) has emerged as a powerful approach for retrieving the phase information by using the far-field diffraction intensity with an iterative algorithm[11]. CDI has been widely used with a broad range of radiations, including the visible light, high-energy electrons, and x ray photons[12–16]. Like the recently developed CDI method, the coherent modulation imaging (CMI) method[17–22] can reconstruct a general complex-valued wave field from a single diffraction pattern. It converges rapidly with a convergent illumination and has a less stringent dynamic range requirement on detectors. The standard phase retrieval process of CMI requires a constraint on the wave field with the hybrid input–output (HIO) algorithm at the "entrance plane," which is essentially the focal plane of the illumination on the sample[17,23]. Thus, a lens is required to form a convergent illumination. A random phase plate (RPP) is placed behind the illumination focus to modulate the wave to be measured, and a CCD is used to record the diffraction pattern. In Ref. [17], a lens ($f = 50$ mm) was used to form the convergent laser beam, and for imaging with an x ray, the converging illumination can only be generated by using a zone plate together with the beam stop, the order-sorting aperture, and other accessories[13], so the experimental setup will be complex. In addition, since the beam stop blocks the central part of the x ray beam and only the first-order diffraction of the zone plate can illuminate the sample after passing the order-sorting aperture, only a small ratio of the x ray energy fluence is applied for the imaging[24–26]. On the other hand, since the radiation from most of synchrotron sources is roughly a parallel beam, the application of the parallel beam directly for CMI imaging is obviously important in consideration of the experimental setup complexity and the usage efficiency of the beam energy. A lens-free CMI is proposed in this Letter, and a set of experiments with lasers was conducted to demonstrate its feasibility.

Figure 1 shows the schematic of the lens-free CMI method. A parallel incident beam passes through the sample and then illuminates the RPP to form a diffraction pattern at the CCD camera. Compared to the current CMI technique, which uses a focused beam for the illumination, this setup is remarkably simplified, especially in terms of the x ray imaging. Since there are no focal spots and the so-called "entrance plane" in Fig. 1, the

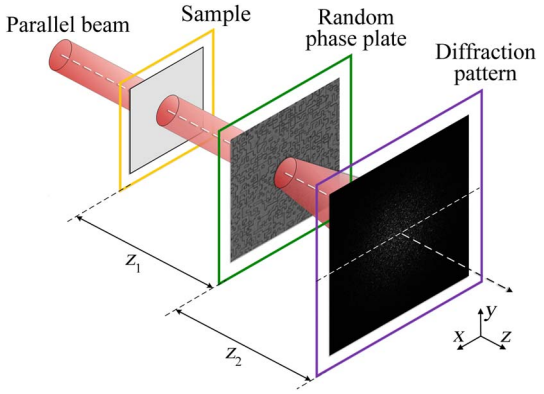

Fig. 1. Schematic of lens-free CMI method.

HIO-based spatial constraint cannot be adopted directly in the reconstruction process. However, according to the principle of Fourier optics, the focal spot on the "entrance plane" of the current CMI is essentially the Fourier Transform of the exit wave field of the object in Fig. 1. In other words, the constraint adopted on the "entrance plane" of the current CMI can be replaced by doing a Fourier transform on the exit field of the sample of Fig. 1 and adopting the constraint on the obtained spatial Fourier components. The underlying physics of the constraint used for Fig. 1 are the same as that of the current CMI, except that the optical Fourier transform is replaced by a numerical Fourier transform.

If the constraint function is assumed as a circular aperture S and the RPP has a known transmission function $O(x, y)$, the reconstruction of the exit wave field can be done iteratively as follows, starting with a random initial guess for the exiting wave field $\varphi_n(x, y)$ of the sample, where n stands for the number of iterations:

(1) Make a fast Fourier transform (FFT) of $\varphi_n(x, y)$ as $\psi_n(u, v) = \mathrm{FFT}[\varphi_n(x, y)]$. A constraint function of circular aperture $S_n = \{^{1,\ 0\le r\le r_n}_{0,\ \ r>r_n}$ is adopted at the obtained Fourier components, where r_n is the radius of the circular aperture, and initially, r_n $(n = 1)$ is a small constant of the order of microns. The Fourier components become $\psi_{c,n}(u, v) = \psi_n(u, v) \cdot S_n$. Then, the improved exiting wave field of the sample is obtained by the inverse Fourier transform $\varphi_{e,n}(x, y) = \mathrm{FFT}^{-1}[\psi_{c,n}(u, v)]$, where n represents the nth iteration.

(2) Propagate $\varphi_{e,n}(x, y)$ to the modulator plane $P_{m,n}(x, y) = \Im[\varphi_{e,n}(x, y), z_1]$, where $\Im$ represents the propagation process.

(3) The exiting wave function of the RPP is $\varphi_{m,n}(x, y) = P_{m,n}(x, y) \cdot O(x, y)$, where $O(x, y)$ is the transmittance function of the designed RPP.

(4) Propagate the exit wave function to the detector plane as $\phi_{m,n}(x, y) = \Im[\varphi_{m,n}(x, y), z_2]$ and replace the amplitude of the wave function with the square root of the recorded diffraction pattern intensity $\phi_{c,n}(x, y) = \sqrt{I}\exp[i\arg|\phi_{m,n}(x, y)|]$, where $\arg|\phi_{m,n}(x, y)|$ represents the phase of $\phi_{m,n}(x, y)$.

(5) The updated wave function $\phi_{c,n}(x, y)$ is propagated back to the RPP plane as $\varphi_{c,n}(x, y) = \Im^{-1}[\phi_{c,n}(x, y), z_2]$, where $\Im^{-1}$ represents the back propagation process.

(6) Update the illumination function on the RPP as

$$P_{\mathrm{new}}(x, y) = P_{m,n}(x, y) + \frac{|O(x, y)|}{|O(x, y)|_{\max}} \frac{O(x, y)^*}{[|O(x, y)|^2 + \alpha]} \times [\varphi_{c,n}(x, y) - P_{m,n}(x, y) \cdot O(x, y)],$$

where $\alpha = 0.5$ is an appropriately chosen constant to suppress the noise[27].

(7) Back propagate $P_{\mathrm{new}}(x, y)$ to the sample plane $\varphi'_{e,n}(x, y) = \Im^{-1}[P_{\mathrm{new}}(x, y), z_1]$.

(8) The new Fourier spectrum is obtained by taking an FFT of $\varphi'_{e,n}(x, y)$ as $\psi'_{c,n}(u, v) = \mathrm{FFT}[\varphi'_{e,n}(x, y)]$. Increase the value of r_n by 0.1 μm in each iteration and update the spectrum with the HIO algorithm[23] as

$$\psi_{c,n+1}(u, v) = \psi'_{c,n}(u, v) \cdot S_{n+1} + \beta[\psi'_{c,n}(u, v) - \psi_{c,n}(u, v)](1 - S_{n+1}),$$

where β takes a value from 0.4 to 0.9[15]. The corresponding exit wave function at the sample plane is $\varphi_{e,n+1}(x, y) = \mathrm{FFT}^{-1}[\psi_{c,n+1}(u, v)]$.

Repeat steps (2)–(8) until the change between two successive iterations of the exit wave field at the sample plane $\varphi_{e,n}(x, y)$ becomes sufficiently small. The hence obtained $\varphi_{e,n}(x, y)$ is regarded as the real exit wave function to be measured. Since the illumination is a parallel beam, $\varphi_{e,n}(x, y)$ actually is the complex transmission function of the sample. Figure 2 is the flowchart of the reconstruction.

The feasibility of the proposed method is verified with experiments using an He–Ne laser. The parallel laser beam transmits the sample and then illuminates the RPP. A CCD camera set at 65 mm behind the RPP is used to record the diffraction patterns. The diameter of the parallel laser beam is 2 mm. The RPP used is a binary RPP with phase values of 0 and π for the He–Ne laser, and its transmission function was premeasured with the extended

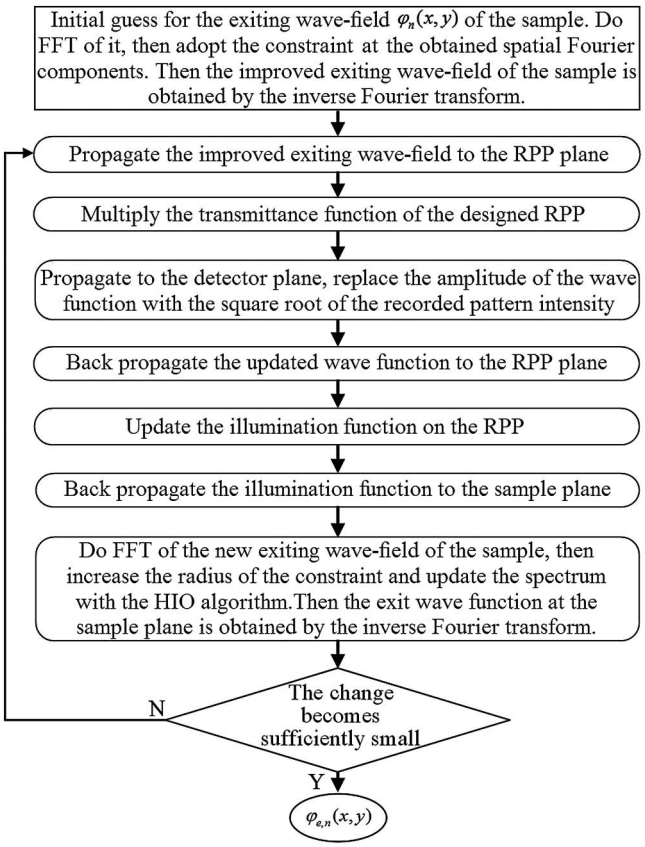

Fig. 2. Flowchart of the proposed method.

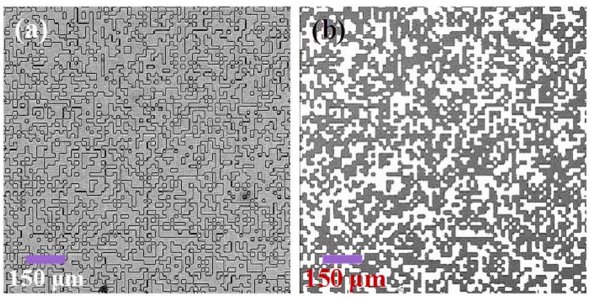

Fig. 3. (a) The amplitude and (b) phase distribution of $O(x, y)$ of the RPP obtained with the ePIE algorithm.

ptychographical iterative engine (ePIE) method[27–29]. The distance between the sample plane and the RPP is 22.26 cm. The wavelength of the laser source used is 632.8 nm, and the CCD used is a PIKE-421B (Allied Vision Technologies, AVT). The CCD has 2048×2048 pixels, and the size of each pixel is $7.4\ \mu\text{m} \times 7.4\ \mu\text{m}$. According to the basic principle of imaging optics, the spatial resolution achievable at the sample plane can be calculated with $\Delta x = (z_1/z_2)\Delta x_D$, where z_1 is the distance between the sample plane and the RPP, z_2 is the distance between the RPP and the detector plane, and $\Delta x_D = 7.4\ \mu\text{m}$ is the size of each pixel of the CCD. In our setup, the resolution is 25.3 μm.

Figures 3(a) and 3(b) show the measured intensity and phase distribution of the RPP with the ePIE algorithm, respectively. The phase values of 0 and π are represented in gray and black, respectively. The size of each diffraction element is $14.8\ \mu\text{m} \times 14.8\ \mu\text{m}$. It can effectively disperse the incident light beam and hence reduce the dynamic range requirement of the detector.

When the incident parallel beam illuminates the RPP, the diffraction pattern recorded by the CCD is shown in Fig. 4(a), where the obvious speckle is due to the random structure of the RPP. With the lens-free CMI algorithm suggested, the illumination on the modulator plane can be reconstructed. Figure 4(b) shows the reconstructed Fourier components of the exit wave field of the sample. Figures 4(c) and 4(d) show the reconstructed modulus and phase on the RPP plane, respectively. Figures 4(e) and 4(f) show the amplitude and the phase of the exit field of the sample. The amplitude clearly shows the edge of the laser beam, and the phase is purely flat.

The diffraction pattern recorded when a biological specimen (a pumpkin stem) was used as the sample is shown in Fig. 5(a). The corresponding reconstructed Fourier components of the exit wave of the sample are shown in Fig. 5(b). The obvious change in the distribution is due to the disturbance of the incident light field by the biological specimen. Figures 5(c) and 5(d) show the amplitude and phase of illumination on the RPP plane, respectively. The amplitude and phase distribution of the reconstructed image of the sample are shown in Figs. 5(e) and 5(f), respectively. The structures of the cells are clearly visible.

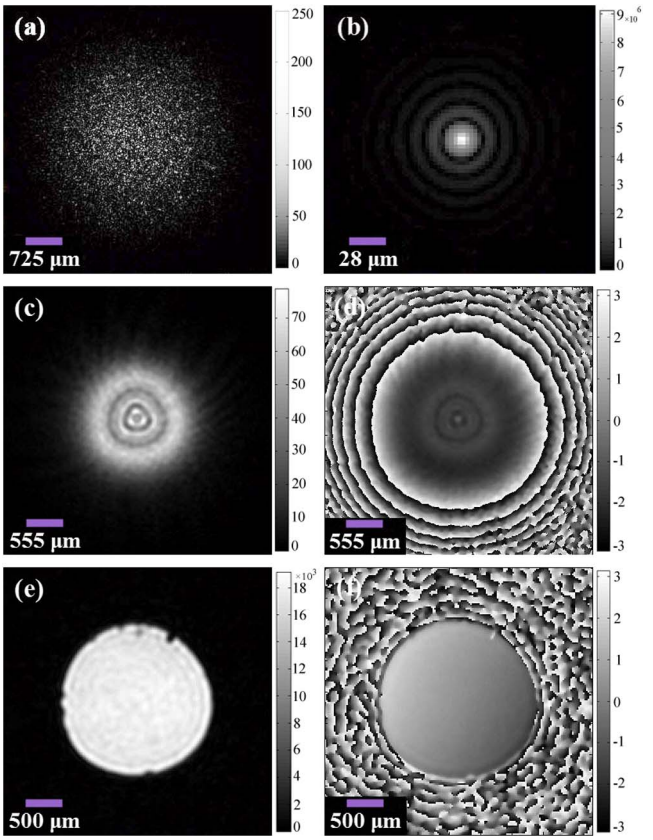

Fig. 4. Recorded diffraction pattern and field reconstructions for the incident beam. (a) The diffraction pattern recorded by CCD, (b) the Fourier components of the exit incident beam, (c) reconstructed amplitude and (d) phase distribution of illumination on the RPP plane. (e) Obtained amplitude and (f) phase distribution of the incident beam.

To evaluate the performance of the proposed method quantitatively, the following error function is calculated on the recorded plane with the ongoing iteration.

$$\text{Error} = \frac{\left||\phi_{m,n}(x, y)| - \sqrt{I}\right|^2}{I}, \tag{1}$$

where $|\phi_{m,n}(x, y)|$ is the modulus of the calculated wave distribution at the CCD plane and I denotes the intensity of the diffraction pattern recorded.

The three convergence curves shown in Fig. 6(a) are the calculated residual errors for $r_n = 0.1\ \mu\text{m}$, $\alpha = 0.5$, and $\beta = 0.4$, 0.6, and 0.9, respectively, and Fig. 6(b) shows three convergence curves for $r_n = 0.1\ \mu\text{m}$, $\beta = 0.6$, and $\alpha = 0.2$, 0.5, and 0.8, respectively. We find that the final residual reconstruction error is much less than 10% after 300 iterations for all these cases. In other words, the dependency of the performance on the values of α and β is quite weak. Fig. 6(c) shows four convergence curves for $\alpha = 0.5$, $\beta = 0.6$ and $r_n = 0.05$, 0.1, 0.2, and 0.3 μm, respectively. From the four curves, we can find that here, $r_n = 0.1\ \mu\text{m}$ is a suitable parameter chosen to improve the convergence speed.

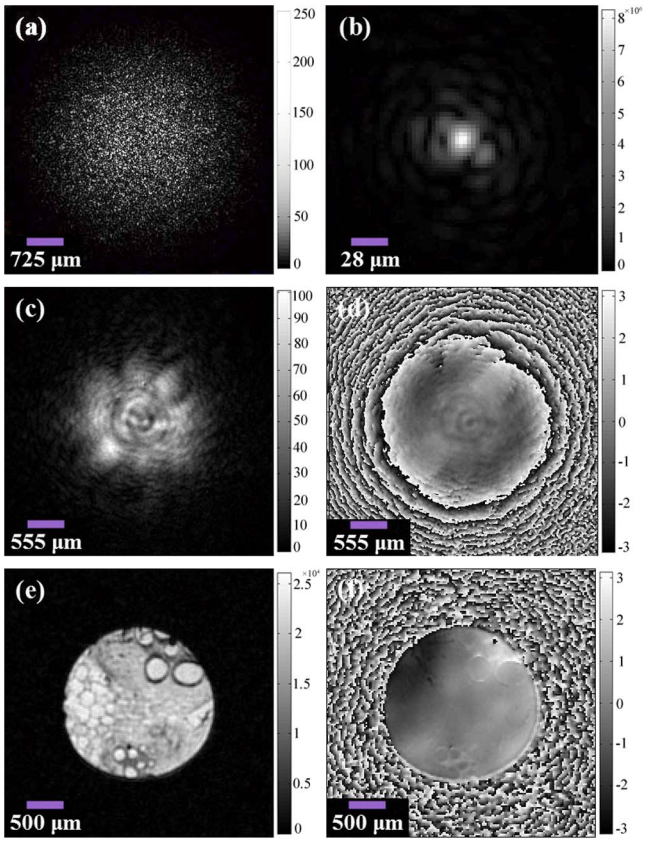

Fig. 5. Recorded diffraction pattern and reconstructed fields when a biological specimen (a pumpkin stem) is used as the sample. (a) The diffraction pattern recorded by CCD, (b) the Fourier components of the exit wave field of the sample, (c) the reconstructed amplitude, and (d) the phase distribution of illumination on the RPP. The reconstructed (e) amplitude and (f) phase distribution of the sample.

The spatial resolution capability of the proposed lensfree CMI method is measured by imaging a United States Air Force (USAF) 1951 target. Figures 7(a) and 7(b) show the amplitude and the phase distribution of the

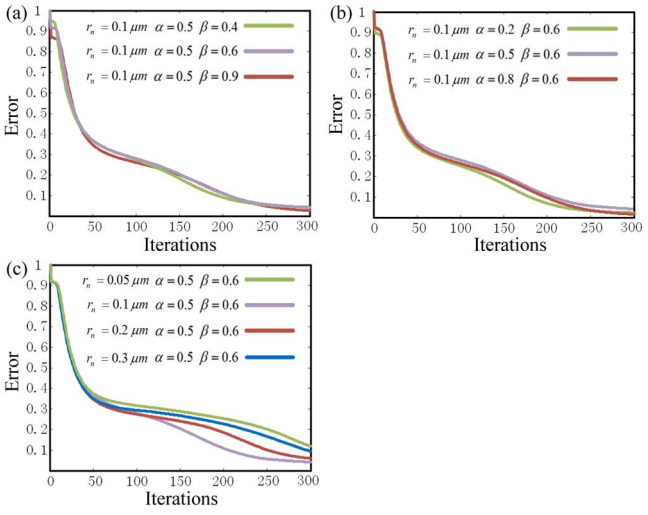

Fig. 6. Convergence curves obtained as a function of the number of iterations with different parameters of r_n, α, and β.

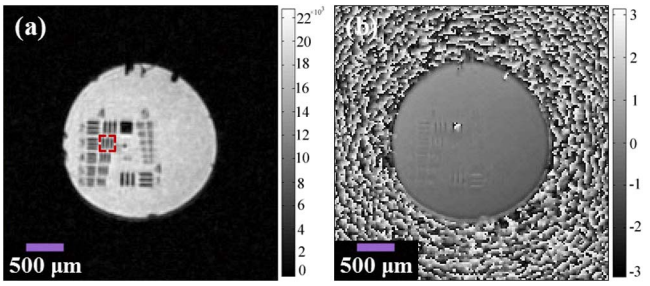

Fig. 7. USAF 1951 target is placed at the sample plane. The reconstructed (a) amplitude and (b) phase distribution of the transmitted field of the USAF 1951 target.

transmitted field of the sample, respectively, where we can find that the resolution achieved is about 24.8 μm, which agrees with the calculated spatial resolution of 25.3 μm.

In conclusion, we experimentally demonstrate a lensfree CMI method to realize the measurement of a complex-valued wave field with a single diffraction pattern. By illuminating the sample with the parallel beam and adopting constraints on the Fourier transform of the exit wave of sample, the converging lens or zone plate, and additional accessories, which remarkably increase the complexity of the experimental setup and lead to energy fluence loss, are no longer required. The feasibility of the proposed method is verified by experiments with a laser beam.

This work was supported by the Foundation (No. 29201431151100301) and the One Hundred Person Project of the Chinese Academy of Sciences, China (No. 902012312D1100101).

References

1. K. A. Nugent, T. E. Gureyev, D. F. Cookson, D. Paganin, and Z. Barnea, Phys. Rev. Lett. **77**, 2961 (1996).
2. P. Rejmánková-Pernot, P. Cloetens, J. Baruchel, J. P. Guigay, and P. Moretti, Phys. Rev. Lett. **81**, 3435 (1998).
3. K. A. Nugent, A. G. Peele, H. N. Chapman, and A. P. Mancuso, Phys. Rev. Lett. **91**, 203902 (2003).
4. H. Itoh, K. Nagai, G. Sato, K. Yamaguchi, T. Nakamura, T. Kondoh, C. Ouchi, T. Teshima, Y. Setomoto, and T. Den, Opt. Express **19**, 3339 (2011).
5. A. Anand, V. K. Chhaniwal, P. Almoro, G. Pedrini, and W. Osten, Opt. Lett. **34**, 1522 (2009).
6. Y. Li, W. Xiao, F. Pan, and L. Rong, Chin. Opt. Lett. **12**, 020901 (2014).
7. P. W. M. Tsang, Y. T. Chow, and T.-C. Poon, Chin. Opt. Lett. **13**, 060901 (2015).
8. W. J. Wild, Opt. Lett. **23**, 573 (1998).
9. A. Anand, G. Pedrini, W. Osten, and P. Almoro, Opt. Lett. **32**, 1584 (2007).
10. H. Wang, C. Liu, X. He, X. Pan, S. Zhou, R. Wu, and J. Zhu, High Power Laser Sci. Eng. **2**, e25 (2014).
11. J. Miao, P. Charalambous, J. Kirz, and D. Sayre, Nature **400**, 342 (1999).
12. H. N. Chapman, A. Barty, M. J. Bogan, S. Boutet, M. Frank, S. P. Hau-Riege, S. Marchesini, B. W. Woods, S. Bajt, W. H. Benner,

R. A. London, E. Plonjes, M. Kuhlmann, R. Treusch, S. Düsterer, T. Tschentscher, J. R. Schneider, E. Spiller, T. Möller, C. Bostedt, M. Hoener, D. A. Shapiro, K. O. Hodgson, D. van der Spoel, F. Burmeister, M. Bergh, C. Caleman, G. Huldt, M. M. Seibert, F. R. N. C. Maia, R. W. Lee, A. Szoke, N. Timneanu, and J. Hajdu, Nat. Phys. **2**, 839 (2006).

13. H. N. Chapman and K. A. Nugent, Nat. Photon. **4**, 833 (2010).
14. S. Roy, D. Parks, K. A. Seu, R. Su, J. J. Turner, W. Chao, E. H. Anderson, S. Cabrini, and S. D. Kevan, Nat. Photon. **5**, 243 (2011).
15. Z. M. Zuo, I. Vartanyants, M. Gao, R. Zang, and L. A. Nagahara, Science **300**, 1419 (2003).
16. I. Robinson and R. Harder, Nat. Mater. **8**, 291 (2009).
17. F. Zhang and J. M. Rodenburg, Physica Rev. B **82**, 121104 (2010).
18. F. Zhang, I. Peterson, J. Vila-Comamala, A. Diaz, F. Berenguer, R. Bean, B. Chen, A. Menzel, I. K. Robinson, and J. M. Rodenburg, Opt. Express **21**, 13592 (2013).
19. X. He, S. P. Veetil, C. Liu, S. Gao, Y. Wang, J. Wang, and J. Zhu, Laser Phys. Lett. **12**, 015005 (2014).
20. H. Tao, S. P. Veetil, J. Cheng, X. Pan, H. Wang, C. Liu, and J. Zhu, Appl. Opt. **54**, 1776 (2015).
21. H. Tao, S. P. Veetil, X. Pan, C. Liu, and J. Zhu, Appl. Opt. **54**, 6632 (2015).
22. X. Pan, S. P. Veetil, C. Liu, H. Tao, Y. Jiang, Q. Lin, X. Li, and J. Zhu, Laser Phys. Lett. **13**, 055001 (2016).
23. J. R. Fienup, Opt. Lett. **3**, 27 (1978).
24. J. Miao, T. Ishikawa, I. K. Robinson, and M. M. Murnane, Science **348**, 530 (2015).
25. R. N. Wilke, M. Priebe, M. Bartels, K. Giewekemeyer, A. Diaz, P. Karvinen, and T. Salditt, Opt. Express **20**, 19232 (2012).
26. W. L. Chao, B. D. Harteneck, J. A. Liddle, E. H. Anderson, and D. T. Attwood, Nature **435**, 1210 (2005).
27. J. M. Rodenburg and H. M. Faulkner, Appl. Phys. Lett. **85**, 4795 (2004).
28. H. M. L. Faulkner and J. M. Rodenburg, Phys. Rev. Lett. **93**, 023903 (2004).
29. A. M. Maiden and J. M. Rodenburg, Ultramicroscopy **109**, 1256 (2009).